

Extended wavelet Galerkin method for mixed-mode cracked FGM plate under static and dynamic loads

Satoyuki Tanaka^{a,*}, Kohei Nakatsuji^a, Hanlin Wang^{a,*}

^a*Graduate School of Advanced Science and Engineering,
Hiroshima University, Higashi-Hiroshima, Japan,
e-mail: satoyuki@hiroshima-u.ac.jp, b190699@hiroshima-u.ac.jp,
hanlinwang@hiroshima-u.ac.jp*

Abstract

The extended wavelet Galerkin method (XWGM) is presented for fracture mechanics analysis of functionally graded material (FGM) cracked plates under static and dynamic loads. The nonhomogeneous stress distribution and stress wave transition can be approximated by the piecewise truncated polynomial (B-spline) functions. The steep stress gradients around the crack tip can be captured by superposing the higher resolution wavelet functions with the nature of multiresolution analysis (MRA) in the wavelet theory. Additionally, a trigonometric function and Heaviside function are employed to enrich the wavelet bases for the fracture modeling. The interaction integral method is utilized to evaluate the static and dynamic mixed-mode stress intensity factors taking the inertia and material nonhomogeneity into account. Applicability of XWGM to the FGM crack problems is discussed through the numerical examples.

Keywords: Wavelet Galerkin Method; Functionally Graded Material; Crack; Fracture Mechanics Parameters

*Corresponding author

1. Introduction

Functionally graded material (FGM) is intensively investigated due to its special characteristics of heterogeneity. Since the material properties are smoothly graded, the sharp material interface is eliminated. Toughness in delamination and fatigue damage resistance are consequently enhanced [1]. Structural integrity of the FGM components under various operational conditions becomes crucial. Therefore, highly accurate and effective analysis methods are required. Fracture mechanics parameters, J-integral and SIFs [2], are useful for the structural integrity assessment. Based on finite element method (FEM), Anlas et al. [3] studied mode-I fracture behavior of the FGM plate. The global material variation was achieved by the combination of many elements with locally homogeneous material properties. Kim and Paulino [4] evaluated two-dimensional (2D) static mixed-mode SIFs of the FGM plates. Song and Paulino [5] further investigated dynamic fracture behaviors.

Apart from the mesh based methodologies, meshfree and particle methods [6-11] are attractive for the fracture analysis of homogeneous and nonhomogeneous materials. The authors have studied mechanical behaviors of plates and shells [12-16] employing reproducing kernel particle method (RKPM) [7] and nodal integration techniques [17-19]. As for application to the FGM, Chen et al. [20] and Rao and Rahman [21] utilized element free Galerkin method [6] to calculate mode-I and mixed-mode SIFs. Sladek et al. [22] proposed a local boundary integral equation in conjunction with moving least squares for mode-I dynamic SIF (DSIF) computation. Shams and Soltani [23] investigated buckling behaviors of the FGM nano-plate by RKPM. Qin et al. [24] further introduced radial basis function into RKPM for the elastodynamics analysis of the FGM structure to improve the accuracy. Bui et al. [25] solved the FGM composite by extended radial point interpolation method. Ozdemir et al. [26] analyzed crack propagation in FGM plate by using ordinary state based peridynamics (OSPD). Meanwhile, the literatures [27-29] gave in-depth investigations of the homogeneous and nonhomogeneous plates in terms of SIFs using OSPD.

A fixed-grid modeling, e.g., voxel-based FEM [30], is considered as one of the meshfree approaches because the model generation process is simplified by the structured grids. However, a local refinement technique is required for the stress concentration region. Subsequently, wavelet-based numerical methods [31-39] are alternative. Wavelet Galerkin method (WGM),

a wavelet-based approach [40-44], uses the equal-spaced structured grids for the discretization. The deformation is interpolated by the wavelet basis functions. The multiresolution analysis (MRA) of the wavelet theory is capable of the local refinement concern by superposing the different length scale wavelet functions on the base model. Therefore, the WGM is considered as an advanced fixed-grid approach.

In the present study, the extended WGM (XWGM) [45] is addressed for analyzing static and dynamic mixed-mode SIFs of a stationary crack in 2D FGM plates. Not only nonhomogeneous stress distribution and stress wave transition but also steep stress gradients around the crack tip are represented based on the truncated polynomial (B-spline) scaling/wavelet functions [46]. Effective fracture modeling is achieved by introducing enrichment functions based on the extended FEM (X-FEM) [47]. The interaction integral method (IIM) considering the inertia and material nonhomogeneity [5] is employed for the fracture mechanics parameter evaluation. The authors analyzed the 2D fracture problems [48,49] but no material nonhomogeneity was considered. Applicability and effectiveness of the proposed method to cracked FGM plates are critically investigated here. Because available SIFs and DSIFs examples for 2D FGM plates are few, a new numerical example is addressed. The fracture mechanics parameters are verified by comparing with another numerical method, OSPD [50].

This paper is organized as follows. In second section, boundary value problem (BVP) of the 2D cracked FGM problems is formulated and discretized by XWGM. A technique to evaluate mixed-mode DSIFs is presented in third section. In fourth section, several numerical examples are demonstrated. Concluding remarks are addressed in the final section.

2. Wavelet Galerkin Method for a Cracked FGM Plate

2.1. Boundary value problem

A 2D cracked FGM plate under dynamic loads is studied as shown in Fig. 1(a). Small strain and small deformation are assumed. x_1 - x_2 and x'_1 - x'_2 are global and local Cartesian coordinate systems, respectively. r and θ are components of local polar coordinate system from the crack tip. \mathbf{x} is a position vector. The domain of the body is Ω with its boundary Γ . Ω consists of a smoothly heterogeneous material. \mathbf{n} is normal to the body. Γ_t is the traction boundary. Γ_u is the essential boundary. $\Gamma = \Gamma_u \cup \Gamma_t$ and $\Gamma_u \cap \Gamma_t = \emptyset$. $\bar{\mathbf{u}}(\mathbf{x}, t)$ and $\bar{\mathbf{t}}$ are prescribed displacement and traction vectors. Ω_{c+} and Ω_{c-}

are upper and lower domains of the crack. Γ_{c+} and Γ_{c-} are top and bottom surfaces of the crack, respectively.

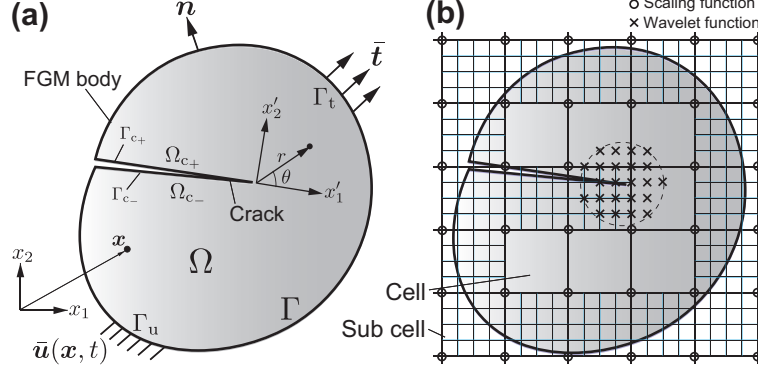


Figure 1: BVP for a 2D cracked FGM and its WG discretization: (a) BVP for 2D cracked FGM, (b) WG discretization with equally spaced structured cell/sub-cells.

The governing equations of the BVP can be written without the body force term, as:

$$\begin{aligned} \rho \ddot{\mathbf{u}} &= \nabla \cdot \boldsymbol{\sigma} & \text{in } \Omega, \\ \boldsymbol{\sigma}^T \cdot \mathbf{n} &= \bar{\mathbf{t}} & \text{on } \Gamma_t, \\ \boldsymbol{\sigma}^T \cdot \mathbf{n} &= 0 & \text{on } \Gamma_{c+} \text{ and } \Gamma_{c-}, \end{aligned} \quad (1)$$

with the essential boundary conditions (BCs), as: $\mathbf{u}(\mathbf{x}, t) = \bar{\mathbf{u}}(\mathbf{x}, t)$ on Γ_u . ρ is density of the material and $\ddot{\mathbf{u}}$ is acceleration. $\nabla \cdot$ is a divergence operator. $\boldsymbol{\sigma}$ is Cauchy stress tensor. The displacement-strain relation is written as $\boldsymbol{\varepsilon} = \nabla^s \mathbf{u}(\mathbf{x}, t)$ with a symmetric part of the displacement gradient ∇^s .

The initial conditions are set as: $\mathbf{u}(\mathbf{x}, t) = \bar{\mathbf{u}}(\mathbf{x}, 0)$ and $\dot{\mathbf{u}}(\mathbf{x}, t) = \dot{\bar{\mathbf{u}}}(\mathbf{x}, 0)$, respectively. $\mathbf{u}(\mathbf{x}, t)$ and $\dot{\mathbf{u}}(\mathbf{x}, t)$ are displacement and velocity vectors at time t . $\bar{\mathbf{u}}(\mathbf{x}, 0)$ and $\dot{\bar{\mathbf{u}}}(\mathbf{x}, 0)$ are the initial values.

The constitutive equation is written considering the smooth heterogeneous property, as: $\boldsymbol{\sigma} = \mathbf{C}(\mathbf{x}) : \boldsymbol{\varepsilon}$. $\mathbf{C}(\mathbf{x})$ depends on Young's modulus $E(\mathbf{x})$ and Poisson's ratio $\nu(\mathbf{x})$ with \mathbf{x} value. For plane stress condition,

$$\mathbf{C}(\mathbf{x}) = \frac{E(\mathbf{x})}{1 - \nu(\mathbf{x})^2} \begin{bmatrix} 1 & \nu(\mathbf{x}) & 0 \\ \nu(\mathbf{x}) & 1 & 0 \\ 0 & 0 & \frac{1 - \nu(\mathbf{x})}{2} \end{bmatrix}, \quad (2)$$

and for plane strain condition, it can be represented as:

$$\mathbf{C}(\mathbf{x}) = \frac{E(\mathbf{x})(1 - \nu(\mathbf{x}))}{(1 + \nu(\mathbf{x}))(1 - 2\nu(\mathbf{x}))} \begin{bmatrix} 1 & \frac{\nu(\mathbf{x})}{1 - \nu(\mathbf{x})} & 0 \\ \frac{\nu(\mathbf{x})}{1 - \nu(\mathbf{x})} & 1 & 0 \\ 0 & 0 & \frac{1 - 2\nu(\mathbf{x})}{2(1 - \nu(\mathbf{x}))} \end{bmatrix}. \quad (3)$$

The strong form in Eq. (1) is transformed into a weak form, as:

$$\rho \int_{\Omega} \delta \mathbf{u}^T \ddot{\mathbf{u}} d\Omega + \int_{\Omega} \nabla^s \delta \mathbf{u} : \boldsymbol{\sigma} d\Omega - \int_{\Gamma_t} \delta \mathbf{u}^T \bar{\mathbf{t}} d\Gamma_t = 0, \quad (4)$$

where $\delta \mathbf{u}$ is the variation of the displacement. For the static case, only the second and third terms of Eq. (1) are employed. A penalty formulation is used for imposing the essential BCs.

The wavelet Galerkin (WG) modeling for the cracked body is illustrated in Fig. 1(b). So far, there are several approaches that have been proposed to analyze the global weak form in Eq. (4), e.g., background cell [6], nodal integration [17], the use of a boundary integral [51-53]. In the present study, a fixed-grid approach is chosen. The equally spaced grids are placed on Ω . A rectangular domain surrounded by the four grid points is called “cell”. The scaling and wavelet functions are employed as the basis functions. The functions are located equidistantly. The cell is further divided into a number of “sub-cells” for the accurate representation of the boundary of the body and the crack segment. The numerical integration of the weak form is carried out based on the cell/sub-cell. The extended wavelet Galerkin (XWG) crack modeling and its discretization are presented in Section 2.4.

2.2. B-spline wavelet bases

Linear, quadratic and cubic B-spline wavelet bases are employed. The functions consist of the truncated polynomials. The linear B-spline scaling/wavelet bases are referred to [45]. The one-dimensional (1D) quadratic and cubic functions are presented in Fig. 2(a) and (b). They are constructed by the two-scale relation and the bi-orthogonality condition in the wavelet theory. A function interpolated by the wavelet bases forms a hierarchical structure of the solution. The mathematical nature is so-called MRA. The property works well in the WG modeling and its discretization. For more detailed descriptions of the wavelet bases, please see [46].

The quadratic B-spline functions with different wave lengths are shown in Fig. 2(c). The lowest resolution level is assumed as level- j . The WG

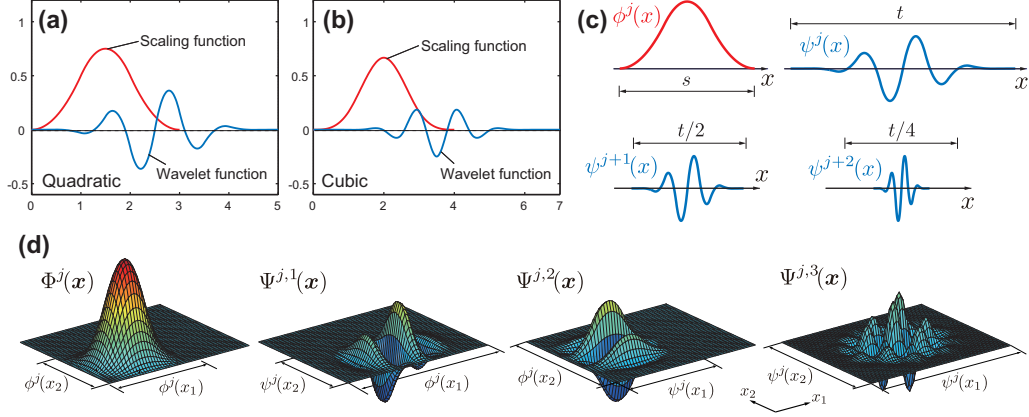


Figure 2: B-spline wavelet bases: (a) 1D Quadratic B-spline, (b) 1D Cubic B-spline, (c) 1D definition of function support to the resolution level (Quadratic B-spline), (d) 2D Level- j scaling/wavelet functions (Quadratic B-spline).

model is called as the level- j model. The level- j scaling function $\phi^j(x)$ is employed in the level- j model. The function span of $\phi^j(x)$ is “ s ”. One step higher resolution model of the level- j model is called the level- $(j+1)$ model. It is developed by superposing the level- j wavelet function $\psi^j(x)$ to the level- j model. The span of $\psi^j(x)$ is “ t ”. Moreover, the level- $(j+1)$ wavelet functions $\psi^{(j+1)}(x)$ are included to the level- $(j+1)$ model to develop the level- $(j+2)$ model. The span of $\psi^{(j+1)}(x)$ and $\psi^{(j+2)}(x)$ are “ $t/2$ ” and “ $t/4$ ”, respectively. Same procedures are taken for higher resolution models. The 2D level- j scaling/wavelet functions are represented in Fig. 2(d). They can be developed by the product of the 1D basis functions.

2.3. Spatial resolution in wavelet Galerkin method

For the WG analysis, two different models are employed. One is uniform refinement (UR) model and the other is multiresolution (MR) model. The 1D level- j , $-(j+1)$ and $-(j+2)$ UR models are respectively shown in Fig. 3(a). The scaling functions are employed equidistantly. The level- j , $-(j+1)$ and $-(j+2)$ cells are respectively used for numerical integration of the stiffness matrix. Gauss quadrature rule is chosen. As the resolution increases, lengths of the cells and scaling functions become half.

The level- j , $-(j+1)$ and $-(j+2)$ MR models are respectively shown in Fig. 3(b). The level- j and $-(j+1)$ wavelet functions are superposed onto the level- j model. With the MRA nature of the wavelet bases, the hierarchical

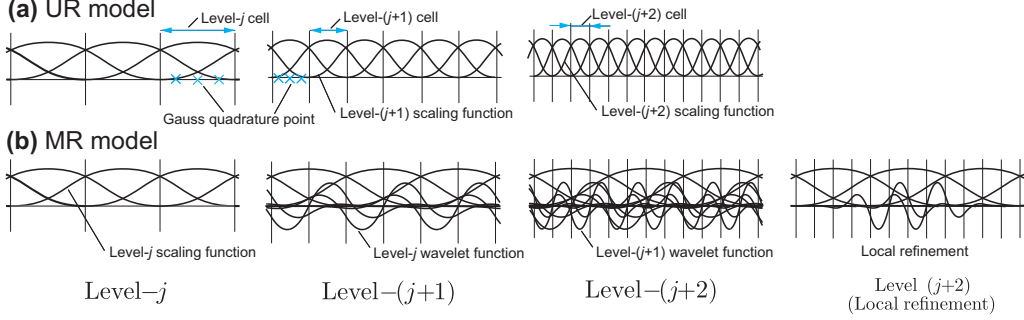


Figure 3: 1D UR and MR models (Quadratic B-spline): (a) UR model, (b) MR model.

structure of the solution can be developed. The local refined level- $(j+2)$ MR model is also presented in Fig. 3(b). By employing the different resolution wavelet functions locally, high-accurate computation is achieved.

2.4. Extended wavelet Galerkin method

For the uncracked WG model, deformation of the level- $(j+1)$ model is approximated by the level- j scaling/wavelet functions, as:

$$\mathbf{u}^{j+1}(\mathbf{x}) = \sum_{k,l} \mathbf{a}_{k,l}^j \Phi_{k,l}^j(\mathbf{x}) + \sum_{i=1}^3 \sum_{k,l} \mathbf{d}_{k,l}^{i,j} \Psi_{k,l}^{i,j}(\mathbf{x}), \quad (5)$$

where $\mathbf{u}^{j+1}(\mathbf{x})$ is the level- j displacement. $\mathbf{a}_{k,l}^j$ and $\mathbf{d}_{k,l}^{i,j}$ are their coefficients. k and l are translation parameters for x_1 - and x_2 -directions that correspond to center position of the basis functions.

For the cracked WG model, the X-FEM concept is introduced [45]. The level- $(j+1)$ displacement can be written in XWGM, as:

$$\begin{aligned} \mathbf{u}^{j+1}(\mathbf{x}) &= \sum_{k,l} \mathbf{a}_{k,l}^j \Phi_{k,l}^j(\mathbf{x}) + \sum_{k,l \in \mathbf{J}_s} \mathbf{b}_{k,l}^j H(\mathbf{x}) \Phi_{k,l}^j(\mathbf{x}) + \sum_{k,l \in \mathbf{C}_s} \mathbf{c}_{k,l}^j \gamma(\mathbf{x}) \Phi_{k,l}^j(\mathbf{x}) \\ &+ \sum_{i=1}^3 \sum_{k,l} \mathbf{d}_{k,l}^{i,j} \Psi_{k,l}^{i,j}(\mathbf{x}) + \sum_{i=1}^3 \sum_{k,l \in \mathbf{C}_w} \mathbf{e}_{k,l}^{i,j} \gamma(\mathbf{x}) \Psi_{k,l}^{i,j}(\mathbf{x}). \end{aligned} \quad (6)$$

The second term of right hand side in Eq. (6) is an enriched term for the scaling functions to represent displacement discontinuity across the crack. \mathbf{J}_s is set of the enriched term. $H(\mathbf{x})$ is Heaviside function, i.e., $H(\mathbf{x})=1$ for Ω_{c+} and $H(\mathbf{x})=-1$ for Ω_{c-} , respectively. The second term is employed when the

crack segment crosses the function support. The third and fifth terms are enriched terms for scaling and wavelet functions to represent severe stress concentration around the crack tip. \mathbf{C}_s and \mathbf{C}_w is a set of the scaling and wavelet functions, respectively. $\gamma(\mathbf{x}) = \sqrt{r} \sin(\theta/2)$ is chosen. These terms are employed when the crack tip is included in the support of the functions. Higher resolution approximation can be achieved by adding the level- $(j+1)$, $-(j+2)$, \dots wavelet functions and their enrichment functions.

The BVP in Eq. (1) is discretized by the XWGM. The level- $(j+1)$ displacement $\mathbf{u}^{j+1}(\mathbf{x})$ in Eq. (6) can be written in matrix form, as:

$$\mathbf{u}^{j+1}(\mathbf{x}) = \mathbf{N}^{j+1} \mathbf{U}^{j+1}. \quad (7)$$

\mathbf{N}^{j+1} is a matrix in terms of the wavelet basis functions. \mathbf{U}^{j+1} is the coefficient vector. They are written, as:

$$\mathbf{N}^{j+1} = [\Phi^j \quad H\Phi^j \quad \gamma\Phi^j \quad \Psi^{1,j} \quad \Psi^{2,j} \quad \Psi^{3,j} \quad \gamma\Psi^{1,j} \quad \gamma\Psi^{2,j} \quad \gamma\Psi^{3,j}], \quad (8)$$

$$\mathbf{U}^{j+1} = (\mathbf{a}^j \quad \mathbf{b}^j \quad \mathbf{c}^j \quad \mathbf{d}^{1,j} \quad \mathbf{d}^{2,j} \quad \mathbf{d}^{3,j} \quad \mathbf{e}^{1,j} \quad \mathbf{e}^{2,j} \quad \mathbf{e}^{3,j})^T, \quad (9)$$

where the functions in the matrix and the coefficients in the vector correspond to each term in Eq. (6). In the similar manner, vectors of the velocity $\dot{\mathbf{u}}^{j+1}(\mathbf{x})$ and acceleration $\ddot{\mathbf{u}}^{j+1}(\mathbf{x})$ are respectively represented, as:

$$\dot{\mathbf{u}}^{j+1}(\mathbf{x}) = \mathbf{N}^{j+1} \dot{\mathbf{U}}^{j+1}, \quad \ddot{\mathbf{u}}^{j+1}(\mathbf{x}) = \mathbf{N}^{j+1} \ddot{\mathbf{U}}^{j+1}. \quad (10)$$

$\dot{\mathbf{U}}^{j+1}$ and $\ddot{\mathbf{U}}^{j+1}$ are their coefficient vectors. Eqs. (7) and (10) are introduced into the weak form of Eq. (4). Following stiffness equation can be obtained, as:

$$\mathbf{M}^{j+1} \ddot{\mathbf{U}}^{j+1} + \mathbf{K}^{j+1} \mathbf{U}^{j+1} = \mathbf{f}^{j+1}, \quad (11)$$

where \mathbf{M}^{j+1} and \mathbf{K}^{j+1} are mass and stiffness matrices for the level- $(j+1)$ model. \mathbf{f}^{j+1} is the force vector. They can be expanded, as:

$$\mathbf{M}^{j+1} = \rho \int_{\Omega} \mathbf{N}^T \mathbf{N} d\Omega, \quad \mathbf{K}^{j+1} = \int_{\Omega} \mathbf{B}^T \mathbf{C} \mathbf{B} d\Omega, \quad \mathbf{f}^{j+1} = \int_{\Gamma_t} \mathbf{N}^T \bar{\mathbf{t}} d\Gamma_t, \quad (12)$$

where $\mathbf{N}(=\mathbf{N}^{j+1})$ is a matrix of the scaling/wavelet functions and $\mathbf{B}(=\mathbf{B}^{j+1})$ is the displacement gradient matrix.

2.5. Time integration method

The Newmark method is adopted. The weak form in Eq. (11) is discretized, as:

$$(\mathbf{M} + \beta \Delta t^2 \mathbf{K}) \ddot{\mathbf{U}}^n = \mathbf{f} - \mathbf{K} \left\{ \mathbf{U}^{n-1} + \Delta t \dot{\mathbf{U}}^{n-1} + \frac{\Delta t^2}{2} (1 - 2\beta) \ddot{\mathbf{U}}^{n-1} \right\}, \quad (13)$$

where \mathbf{M} and \mathbf{K} are the mass and stiffness matrices, and \mathbf{f} is the external force vector. Δt is time interval. The values with the superscripts $n-1$ and n mean previous and current steps for displacement, velocity and acceleration. $\beta=1/4$ is adopted. At $(n+1)$ -th step, vectors of the displacement \mathbf{U}^{n+1} and velocity $\dot{\mathbf{U}}^{n+1}$ are evaluated, as:

$$\mathbf{U}^{n+1} = \mathbf{U}^n + \Delta t \dot{\mathbf{U}}^n + \Delta t^2 \left(\frac{1}{2} - \beta \right) \ddot{\mathbf{U}}^n + \Delta t^2 \beta \ddot{\mathbf{U}}^{n+1}, \quad (14)$$

$$\dot{\mathbf{U}}^{n+1} = \dot{\mathbf{U}}^n + (1 - \delta) \Delta t \ddot{\mathbf{U}}^n + \delta \Delta t \ddot{\mathbf{U}}^{n+1}, \quad (15)$$

where $\delta=1/2$ is taken. Very fine time interval is chosen to obtain stable numerical results in the Newmark method.

3. Fracture parameters evaluation

3.1. J -integral and its domain form

The fracture parameters of a cracked smoothly heterogeneous material are evaluated. The mixed-mode DSIFs for the cracked FGM plate are solved by the IIM. The detail is included in Song and Paulino [5], and the technique is briefly reviewed.

A contour Γ_0 is introduced surrounding a crack tip. An integral is defined [54] with no crack face traction, as:

$$J = \lim_{\Gamma_0 \rightarrow 0} \int_{\Gamma_0} (W \delta_{1j} - \sigma_{ij} u_{i,1}) n_j d\Gamma, \quad (16)$$

where W is a strain energy density, σ_{ij} is stress components. n_j is normal to Γ_0 . $u_{i,1}$ is a spatial derivative of the displacement to the x'_1 -direction. δ_{1j} is Kronecker delta.

Applying Gauss divergence theorem, the contour integral is transformed to an equivalent domain integral (EDI) form [55,56]. It can be written, as:

$$J = \int_A (\sigma_{ij} u_{j,1} - W \delta_{1j}) q_{,j} dA + \int_A (\sigma_{ij} u_{i,1} - W \delta_{1j})_{,j} q dA, \quad (17)$$

displacement u_i^{aux} considering the material nonhomogeneity, i.e.,

$$\varepsilon_{ij}^{\text{aux}} = \frac{1}{2}(u_{i,j}^{\text{aux}} + u_{j,i}^{\text{aux}}), \quad \sigma_{ij}^{\text{aux}} = C_{ijkl}\varepsilon_{kl}^{\text{aux}}. \quad (20)$$

The mode-I and -II SIFs can be derived from the M -integral term in Eq. (19), as:

$$K_{\text{I}} = \frac{E'_{\text{tip}}}{2}M \quad (K_{\text{I}}^{\text{aux}} = 1, K_{\text{II}}^{\text{aux}} = 0), \quad (21)$$

$$K_{\text{II}} = \frac{E'_{\text{tip}}}{2}M \quad (K_{\text{I}}^{\text{aux}} = 0, K_{\text{II}}^{\text{aux}} = 1), \quad (22)$$

where $E'_{\text{tip}} = E_{\text{tip}}$ for the plane stress condition and $E'_{\text{tip}} = E_{\text{tip}}/(1-\nu_{\text{tip}}^2)$ for the plane strain condition. E_{tip} and ν_{tip} are Young's modulus and Poisson's ratio at the crack tip. It is noted that the J -value and the mixed-mode SIFs has following relation as: $J = (K_{\text{I}}^2 + K_{\text{II}}^2)/E'_{\text{tip}}$.

3.3. Extended wavelet Galerkin discretization

Eq. (11) is discretized by the XWGM. A schematic is shown in Fig. 4(b). The scaling functions are located equidistantly. The different resolution scaling/wavelet functions and their enrichment functions whose center position is located within r_e from the crack tip are used. The domain surrounding the crack tip is divided by the equally spaced cells and sub-cells. The cells are employed for the numerical integration of the stiffness matrix. Gauss quadrature is employed. The physical values of strain, stress, density and material parameters are evaluated at each Gauss point.

The cells and sub-cells are utilized for analyzing Eqs. (16) and (19) in the fracture parameter evaluation. A rectangular domain acrossing the circular domain r_d from the crack tip is employed. The domain integral is carried out based on the cells. A plateau-type $q(\mathbf{x})$ function is chosen.

4. Numerical examples

Four numerical examples of homogeneous and FGM cracked plates are presented. First, two static problems are investigated to examine the accuracy of SIFs. Then, a mixed-mode dynamic problem is studied. The DSIFs are compared with the reference solutions. As a final example, a cracked semi-circular side notch FGM plate under static and dynamic loads is studied. The SIFs and DSIFs are verified with another numerical method, OSPD.

The SIFs and DSIFs are normalized by F_i ($=K_i/\sigma\sqrt{\pi a}$) for Sections 4.1, 4.2 and 4.3. F_i ($=K_i/\sigma\sqrt{\pi(a+c)}$) is employed for Section 4.4. a is a crack (half) length and c is a hole radius.

4.1. Mode-I static problem

An edge crack in a rectangular FGM plate under tensile static loading is investigated. The analysis model is shown in Fig. 5(a). L and W are width and height of the plate. $W=1.0$ (mm) and $L/W=8$ are chosen. Applied stress is $\sigma=1.0$ (MPa). a is crack length. $a/W=0.4, 0.5$ and 0.6 are employed. Young's modulus is smoothly varied in the x_1 -direction, i.e., $E(x_1)=E_1e^{\beta x_1}$. $E_1=E(0.0)$ and $E_2=E(1.0)$ giving $\beta=\log(E_2/E_1)$. $E_2/E_1=0.1, 0.2, 1.0, 5.0$ and 10.0 are studied. Poisson's ratio is constant, i.e., $\nu=0.3$. The plane strain condition is assumed. The mode-I SIF K_I is investigated. The results are compared with the reference solutions [4].

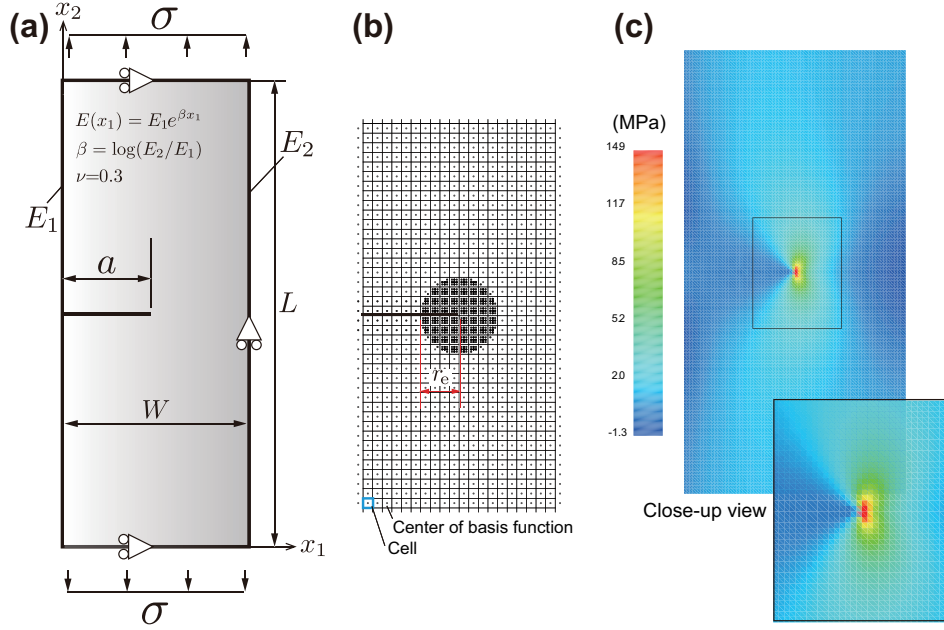


Figure 5: An edge crack in a rectangular FGM plate: (a) Analysis model, (b) Level- $(j+2)$ MR model (Quadratic B-spline), (c) Stress distribution σ_{22} for $E_2/E_1=0.1$ (Quadratic B-spline).

The different resolution UR and MR models are used. The analysis domain is respectively divided by 20×160 , 40×320 and 80×640 equally spaced

cells for the level- j , $-(j+1)$ and $-(j+2)$ UR models. The level- j , $-(j+1)$ and $-(j+2)$ scaling functions are respectively employed. The level- j MR model is equivalent to the level- j UR model. The level- j and $-(j+1)$ wavelet functions as well as their enrichment functions are locally added around the crack tip onto the level- j MR model to develop the level- $-(j+1)$ and $-(j+2)$ MR models. The level- $-(j+2)$ MR model employing quadratic B-spline is shown in Fig. 5(b). $r_e=0.2$ (mm) is chosen. The black points are center position of the scaling/wavelet functions. The rectangular square domain is the cell for the numerical integration. The stress distribution σ_{22} of the level- $-(j+2)$ MR model is drawn in Fig. 5(c). Severe stress concentration can be seen at the crack tip and smooth stress distribution is obtained in the entire analysis domain.

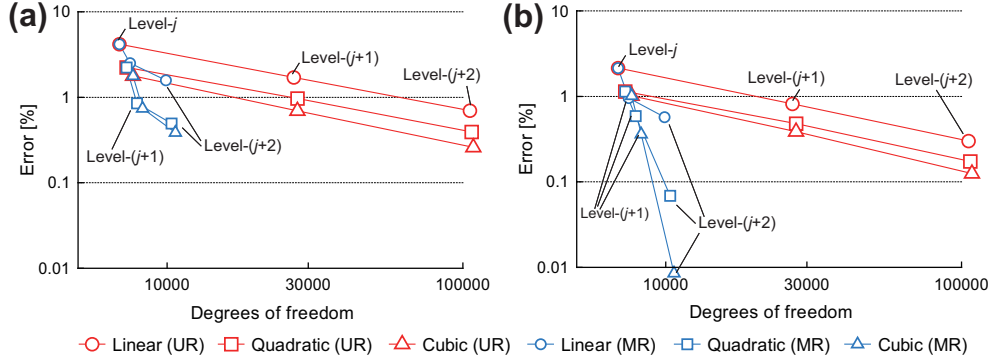


Figure 6: Convergence study of K_I for $a/W=0.5$: (a) $E_2/E_1=0.1$, (b) $E_2/E_1=10$.

Convergence study is carried out for $a/W=0.5$. $r_d=0.4$ (mm) is chosen for evaluating the mode-I SIF extracting from the J -integral employing IIM in Eq. (19). The linear, quadratic and cubic B-spline are employed. The results for $E_2/E_1=0.1$ are shown in Fig. 6(a). The error is defined as: $\text{Error} = |K_I^{\text{Num.}} - K_I^{\text{Ref.}}| / K_I^{\text{Ref.}} \times 100$ (%). $K_I^{\text{Ref.}}$ is taken from [4]. The UR models are uniformly converged to the reference solutions. The convergence rate is similar to the linear, quadratic and cubic B-spline cases, while the error decreases as the higher order B-splines are employed. Additionally, the error drastically reduces when the level- $-(j+1)$ and $-(j+2)$ MR models are employed. The results for $E_2/E_1=10$ is shown in Fig. 6(b). Similar tendency can be seen with $E_2/E_1=0.1$ case.

Based on the numerical studies, the XWG analyses with the quadratic and cubic B-splines provide more accurate results than those of the linear B-

spline. The function support of the quadratic B-spline is smaller than that of the cubic B-spline. The compact support function is easy to handle in the XWG modeling and provides the efficient computation. Therefore, the quadratic B-spline is chosen for the rest of the numerical examples.

A series of computations are carried out for different E_2/E_1 and crack length a/W . The level- $(j+2)$ MR model is chosen. $r_e=0.2$ (mm) and $r_d=0.4$ (mm) are selected. The results are shown in Table 1. The reference values evaluated by J_k^* -integral method [4] are used. All results fit well with the reference solutions. It is confirmed that the XWGM approach is effective for the cracked FGM plate analysis and the SIF evaluation.

Table 1: F_I for different E_2/E_1 and a/W .

E_2/E_1	a/W					
	0.4 (XWGM)	Ref. [4]	0.5 (XWGM)	Ref. [4]	0.6 (XWGM)	Ref. [4]
0.1	2.531	2.544	3.479	3.496	4.930	4.962
0.2	2.420	2.431	3.278	3.292	4.642	4.669
1	2.105	2.110	2.814	2.822	4.014	4.030
5	1.747	1.749	2.362	2.366	3.438	3.448
10	1.588	1.588	2.173	2.175	3.205	3.212

4.2. Mixed-mode static problem

An inclined edge crack in a FGM plate is studied under static tensile load. The analysis model is shown in Fig. 7(a). W is 1.0 (mm). The height to width ratio of the plate is $L/W=2.0$. The crack length is $a/W=0.4\sqrt{2}$ and the inclined angle is $\pi/4$ (rad.). This is a mixed-mode problem. The plane stress condition is assumed. Young's modulus is $E(x_1)=e^{\beta(x_1-0.5)}$ in the x_1 -direction. β is varied 0, 0.1, 0.25, 0.5, 0.75 and 1.0. Poisson's ratio is constant with $\nu=0.3$. The bottom of the plate is fixed in the x_2 -direction and pressure $\sigma(x_1)=e^{\beta(x_1-0.5)}$ (MPa) is applied to the top of the plate. The analysis domain is divided into 25×50 cells for the level- j MR model.

The level- j , $-(j+1)$ and $-(j+2)$ MR models are employed. The XWG results are compared with the reference solutions included in [4] and [21]. The level- $(j+2)$ MR model is shown in Fig. 7(b). $r_e=0.15$ (mm) is chosen. And, the stress distribution σ_{22} for $\beta=0.5$ employing the level- $(j+2)$ MR model is presented in Fig. 7(c). Severe stress concentration and smooth stress distribution can be captured as well as the mode-I case in Fig. 5(c).

Path independency of the SIFs is studied first. F_i is evaluated employing IIM in Eq. (19) by changing the path radius r_d . $r_e=0.15$ (mm) is selected.

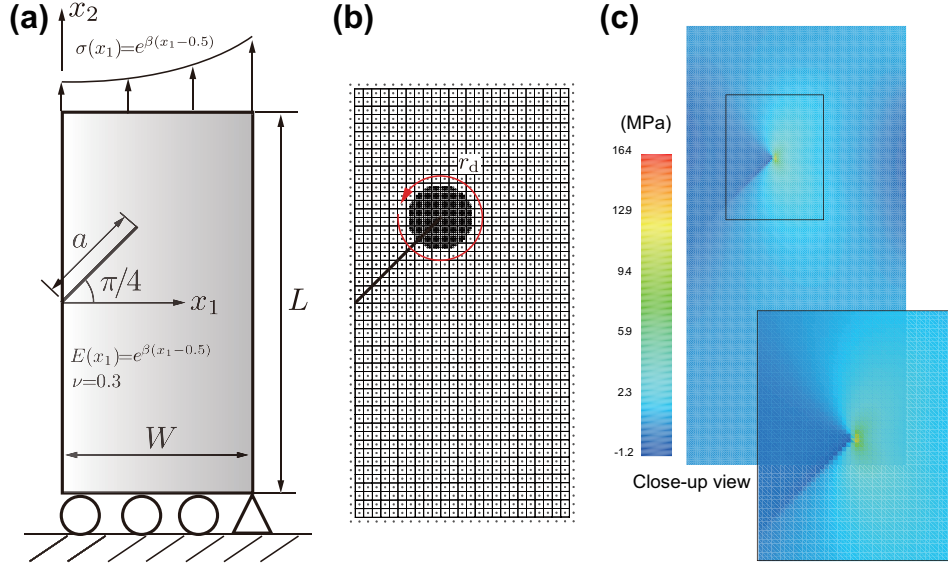


Figure 7: An inclined edge crack in a FGM plate under static load: (a) Analysis model, (b) Level-($j+2$) MR model, (c) Stress distribution σ_{22} for $\beta=0.5$ (Level-($j+2$) MR model).

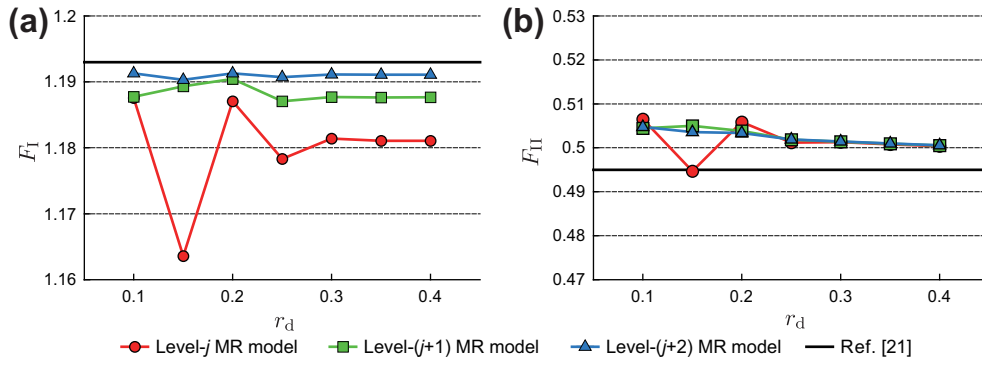


Figure 8: Path independency for mixed-mode problem: (a) F_I , (b) F_{II} .

The results are shown in Fig. 8(a) and (b) for F_I and F_{II} , respectively. Oscillation of the results can be seen for $r_d \leq r_e$ cases as shown in Fig. 8(a). The wavelet functions do not have so-called Partition of Unity (PU) condition. The lack of PU condition may induce the oscillation of SIFs. This problem can be seen in X-FEM and was discussed in [58-60]. The path independency is satisfied as the radius becomes large ($r_d > r_e$). Additionally, the oscillation in SIFs are reduced when the higher resolution WG models are employed. For F_{II} case in Fig. 8(b), similar tendency can be seen with F_I case.

The mixed-mode SIFs are examined by changing β . The level- $(j+2)$ MR model is employed and compared with the reference solutions. $r_d=0.4$ (mm) is chosen. The results are shown in Table 2. For all cases, the XWG results fit well with the reference solutions. It is also confirmed that XWG is competent to perform the high-accurate fracture mechanics computation for mixed-mode cracked problems of the FGM plates.

Table 2: Normalized mixed-mode SIFs for different β .

β	F_I (XWGM)	F_I [4]	F_I [21]	F_{II} (XWGM)	F_{II} [4]	F_{II} [21]
0	1.444	1.451	1.448	0.616	0.604	0.610
0.1	1.389	1.396	1.392	0.590	0.579	0.585
0.25	1.310	1.316	1.313	0.555	0.544	0.549
0.5	1.191	1.196	1.193	0.501	0.491	0.495
0.75	1.084	1.089	1.086	0.453	0.443	0.447
1.0	0.989	0.993	0.990	0.410	0.402	0.405

4.3. Mixed-mode dynamic problem

Mixed-mode crack problem is studied for dynamic loading as well. As shown in Fig. 9(a), a rectangular plate with two cracks emanating from a hole is studied. The width and height are $2W=30$ (mm) and $2H=60$ (mm), respectively. Hole radius is $r=3.75$ (mm). The crack length is $2a=15$ (mm). The inclined angle is $\pi/6$ (rad.). For the level- j MR model, the analysis domain is divided into 40×80 equally spaced cells. Homogeneous material and FGM cases are studied. The plane strain condition is assumed.

4.3.1. Homogeneous material case

To examine the accuracy of the XWG model, static SIFs are investigated first. Young's modulus is $E=199.992$ (GPa) and Poisson's ratio is $\nu=0.3$. Uniform pressure $\sigma=1.0$ (MPa) is applied on the top and bottom plate edges as shown in Fig. 9(a). The level- $(j+2)$ MR model is employed. The model

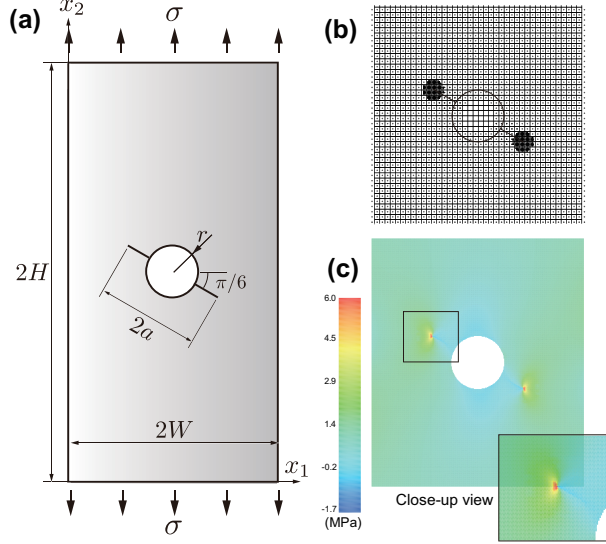


Figure 9: A rectangular plate with two cracks emanating from a hole: (a) Analysis model, (b) Level- $(j+2)$ model, (c) Stress distribution σ_{22} (Homogeneous material case).

is presented in Fig. 9(b). The stress distribution σ_{22} is also presented in Fig. 9(c). The sub-cell approach is adopted to model the hole. $r_e=1.5$ (mm) is employed. Smooth stress distribution can be obtained.

For the reference solution, X-FEM option in Code_Aster [61] is employed. Linear triangle element is employed. The element size near the crack tip is around 0.03125 (mm), and 1.0 (mm) for the entire model. G -theta method [62], SIF evaluation option in Code_Aster, is utilized. Three contours are taken surrounding the crack tip and the values are averaged. $r_d=3.5$ (mm) is selected for the XWGM analysis. The results are $F_I^{\text{XWGM}}=0.948$ and $F_{II}^{\text{XWGM}}=-0.418$, respectively. For the reference solution evaluated by Code_Aster, $F_I^{\text{Ref.}}=0.943$ and $F_{II}^{\text{Ref.}}=-0.416$. The results of the XWGM model and with Code_Aster are almost same and high-accurate SIFs are achieved for the static loading case.

The dynamic case is investigated. $\rho=5,000$ (kg/m³) is used. A step load $\sigma=1.0$ (MPa) is applied to the top and bottom edges of the plate for $t>0$. As for the XWGM model, the analysis condition and the material parameters are same as the linear static case. The computation is carried out until 20 (μ s). The DSIF results presented in [5] are digitized and employed as the reference solutions. The right crack tip DSIFs are shown in Fig. 10. The symbol

marks are the XWGM results and the solid lines are the reference solutions. The XWGM results fit well with the reference solutions for all time steps. It is confirmed that the dynamic analysis and the DSIF evaluation of the XWGM modeling work well for the homogeneous material case.

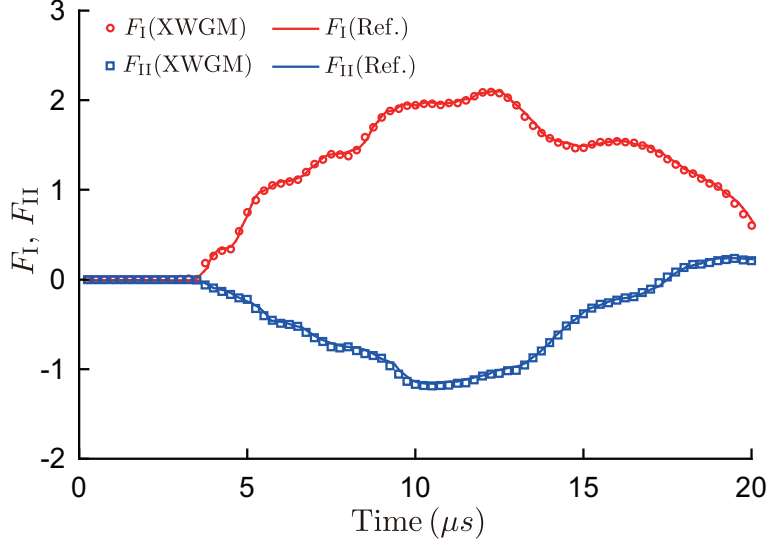


Figure 10: Mixed-mode DSIFs for the right crack tip (Homogeneous material case).

4.3.2. FGM case

The FGM case is investigated. Young's modulus $E(x_1)$ and the density of the material $\rho(x_1)$ are varied to the x_1 -direction, as:

$$E(x_1) = (244x_1 + 7471) \text{ (MPa)}, \quad (23)$$

$$\rho(x_1) = (28.8x_1 + 1380) \text{ (kg/m}^3\text{)}, \quad (24)$$

while Poisson's ratio is constant with $\nu=0.3$. The problem was analyzed in [50]. The computation is performed until 40 (μs). The results are shown in Fig. 11 for the left and right crack tips. All the results fit well with the reference solution. Therefore, it is confirmed that the XWG approach is effective for mixed-mode DSIFs evaluation of the FGM model.

4.4. A crack emanating from semi-circular side notch in a rectangular plate

An edge crack in a semi-circular side notch plate is analyzed for static and dynamic loads. The target problem is shown in Fig. 12(a). The plate width

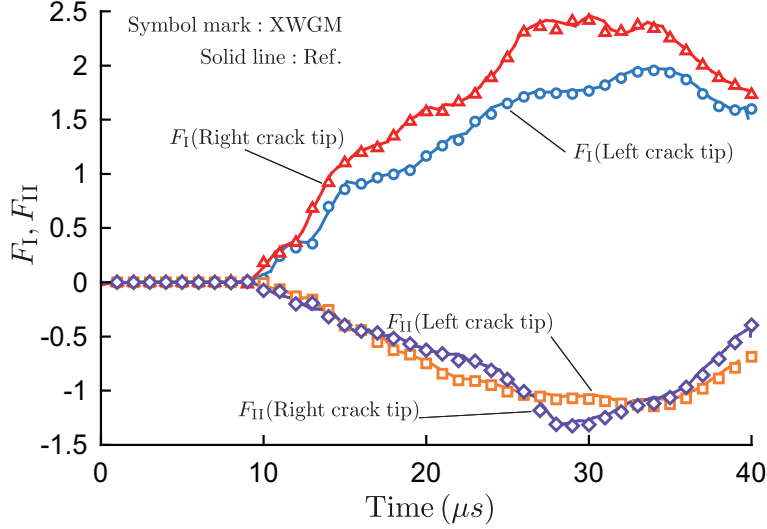


Figure 11: Mixed-mode DSIFs for the left and right crack tips (FGM case).

is $W=30$ (mm) and the height is $2H=60$ (mm). The radius of the semi-circular hole is $c=7.5$ (mm). The crack length is $a=7.5$ (mm). Three cases with various crack inclined angles $\theta=0, \pi/6$ and $\pi/3$ (rad.) are respectively investigated. Poisson's ratio is set as $\nu=0.3$. The mixed-mode SIFs and DSIFs are examined for the homogeneous and FGM cases.

No reference solutions are available for this case study. The fracture parameters are examined with another numerical method, i.e., OSPD. Wang et al. [50] developed SIFs and DSIFs evaluation technique employing OSPD and IIM with the peridynamic differential operator. The related techniques can be seen in [63]. In the OSPD method, the plate is uniformly discretized by 500 and 1,000 divisions in x_1 - and x_2 -direction except the hole region, respectively. Therefore, the grid space is 0.06 (mm) to maintain the numerical accuracy.

The static SIFs are analyzed first. Young's modulus of the homogeneous case is $E=199.992$ (GPa). Eq. (23) is employed for the FGM case. The level- $(j+2)$ model is shown in Fig. 12(b) for $\theta=\pi/3$ (rad.). $r_e=2.0$ (mm) and $r_d=7.0$ (mm) are chosen. The stress distribution σ_{22} of FGM case is shown in Fig. 12(c). Stress concentration can be seen at the crack tip and the hole edge. Smooth stress distribution can be obtained entirely in the analysis domain. The adaptive dynamic relaxation technique [64,65] is employed for the static analyses.

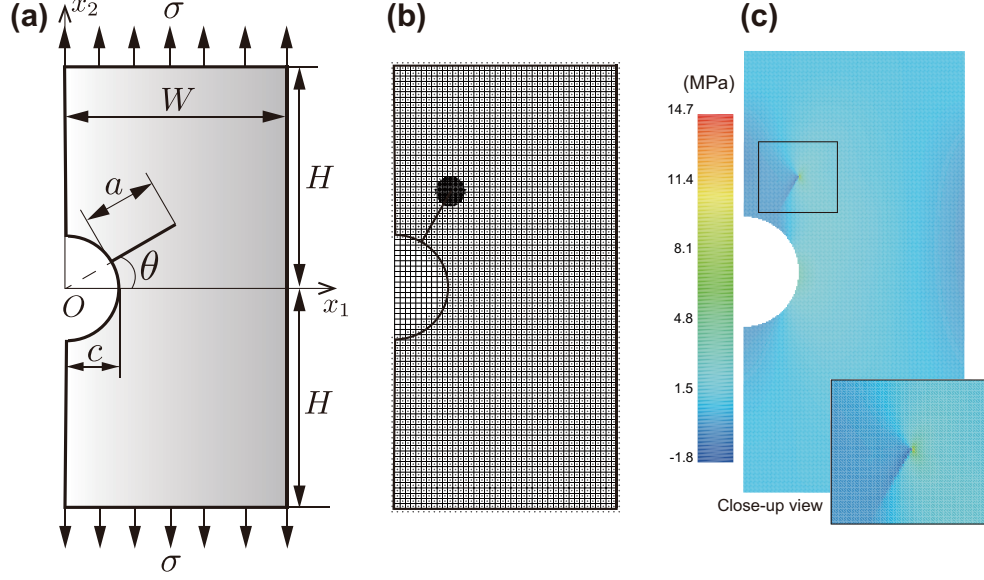


Figure 12: An edged crack in a semi-circular side notch plate: (a) Analysis model, (b) Level- $(j+2)$ model ($\theta=\pi/3$), (c) Stress distribution σ_{22} (FGM case).

The normalized SIFs are shown in Table 3. The overall results are in good agreement. However, there are some differences for mode-II case of the homogeneous material and FGM cases. In the OSPD formulation, the deformation mainly relies on the bond extension and compression, but the bond rotation is not simulated precisely [66,67]. Therefore, the shear deformation is described with relatively low accuracy, especially for the large inclined angles.

Table 3: Mixed-mode SIFs for homogeneous and FGM cases for $\theta=0, \pi/6$ and $\pi/3$ (rad.).

	F_I (Homo.)	F_{II} (Homo.)	F_I (FGM)	F_{II} (FGM)
XWGM ($\theta=0$)	2.819	0.000	2.642	0.000
OSPD	2.807	0.000	2.661	0.000
XWGM ($\theta=\pi/6$)	1.935	0.532	1.819	0.468
OSPD	1.931	0.529	1.827	0.509
XWGM ($\theta=\pi/3$)	0.676	0.404	0.645	0.363
OSPD	0.679	0.407	0.634	0.395

The DSIFs are investigated. Poisson's ratio is constant with $\nu=0.3$, while Young's modulus and the density of the plate are varied along x_1 -direction

based on Eqs. (23) and (24). The mixed-mode DSIFs of the different crack angles $\theta=0, \pi/6$ and $\pi/3$ (rad.) are presented in Fig. 13(a) and (b) for the homogeneous material case. The computation is carried out until 20 (μ s). For $\theta=0$ (rad.) case, a pure mode-I DSIF is evaluated. The mixed-mode DSIFs are evaluated for $\theta=\pi/6$ and $\pi/3$ (rad.). The smaller the inclined angle, the larger the F_I value. For $\theta=\pi/6$ and $\pi/3$ (rad.) cases, mode-II is significant. Since the first stress arrives earlier as the inclined angle becomes larger, the increase timing of F_I also comes earlier. For all cases, XWGM provides a good agreement with the OSPD results.

The FGM computation is carried out until 40 (μ s). The results are shown in Fig. 13(c) and (d) for the mode-I and -II DSIFs, respectively. As well as the homogeneous material case, the mode-I DSIF is evaluated for $\theta=0$ (rad.) case. As the inclined crack angle increases, F_I becomes small for all time steps. The mixed-mode DSIFs are evaluated for $\theta=\pi/6$ and $\pi/3$ (rad.). A good relevancy is obtained between XWGM and OSPD approaches especially for mode-I DSIFs. However, mode-II DSIFs are slightly different for the above two methods. Finally, it can be said that XWGM is capable of providing the proper SIFs and DSIFs for the FGM plate studies.

5. Conclusion

The mixed-mode SIFs and DSIFs of the homogeneous and FGM cracked plates are investigated employing XWGM. Linear, quadratic and cubic B-spline wavelet bases are employed and the numerical accuracy are examined. Through the numerical examples, the quadratic B-spline wavelet bases fit well with for the SIFs and DSIFs evaluations due to high order approximation and compact support property. By introducing the high order wavelet bases enriched with a sinusoidal function, highly accurate SIFs and DSIFs are evaluated. Both static and dynamics fracture analyses are successfully carried out and high-accurate fracture parameters are obtained. Additionally, the semi-circular side notch FGM cracked plate under static and dynamic loading conditions are studied. The results are compared with OSPD and a good agreement is obtained between the XWGM and the OSPD. Finally, it is confirmed that the XWGM combined with the IIM approach is a reliable tool for analyzing SIFs and DSIFs of the FGM plates.

Fracture responses of FGM plates are very important for engineering application and it is a challenging task, especially for the dynamic crack propagation (CP) behaviors, e.g., CP direction and CP speed [68]. The com-

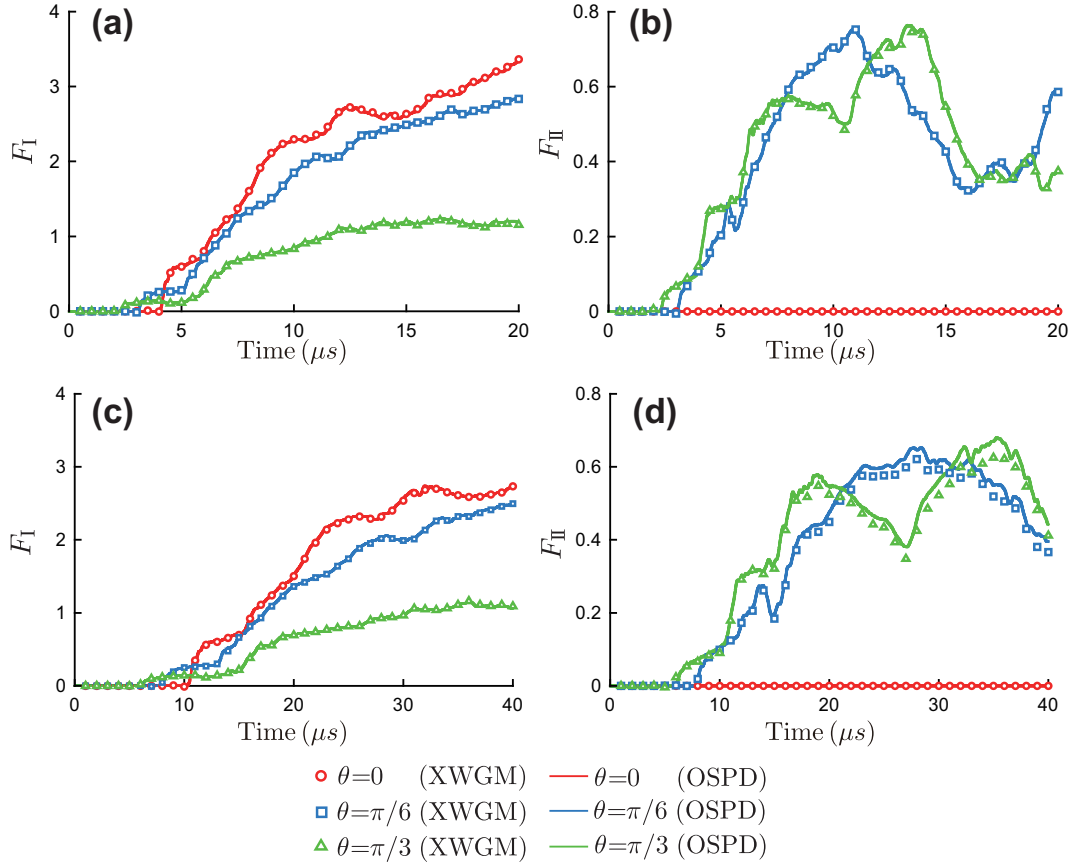


Figure 13: Mixed-mode DSIFs for $\theta=0, \pi/6$ and $\pi/3$ (rad.): (a) F_I (Homogeneous), (b) F_{II} (Homogeneous), (c) F_I (FGM), (d) F_{II} (FGM).

plicated mechanical phenomena should be clarified numerically employing the present approach as well as classical theory [69,70] and other advanced numerical methods, FEM [71], PD [72] and phase field modeling [73].

References

- [1] F. Erdogan, Fracture mechanics of functionally graded materials, *Compos. Eng.* 5 (1995) 753-770.
- [2] G.R. Irwin, Analysis of stresses and strains near the end of a crack traversing a plate, *ASME. J. Appl. Mech.* 24 (1957) 361-364.
- [3] G. Anlas, M.H. Santare, J. Lambros, Numerical calculation of stress intensity factors in functionally graded materials, *Int. J. Fract.* 104 (2000) 131-143.
- [4] J.H. Kim, G.H. Paulino, Finite element evaluation of mixed mode stress intensity factors in functionally graded materials, *Int. J. Numer. Methods Eng.* 53 (2002) 1903-1935.
- [5] S.H. Song, G.H. Paulino, Dynamic stress intensity factors for homogeneous and smoothly heterogeneous materials using the interaction integral method, *Int. J. Solids Struct.* 43 (2006) 4830-4866.
- [6] T. Belytschko, Y.Y. Lu, L. Gu, Element-free Galerkin methods, *Int. J. Numer. Methods Eng.* 37 (1994) 229-256.
- [7] W.K. Liu, S. Jun, Y.F. Zhang, Reproducing kernel particle methods, *Int. J. Numer. Methods Fluids* 20 (1995) 1081-1106.
- [8] T. Rabczuk, T. Belytschko, Cracking particles: a simplified meshfree method for arbitrary evolving cracks, *Int. J. Numer. Methods Eng.* 61 (2004) 2316-2343.
- [9] T. Rabczuk, G. Zi, S. Bordas, H. Nguyen-Xuan, A simple and robust three-dimensional cracking-particle method without enrichment, *Comput. Methods Appl. Mech. Eng.* 199 (2010) 2437-2455.
- [10] J.G. Wang, G.R. Liu, A point interpolation meshless method based on radial basis functions, *Int. J. Numer. Methods Eng.* 54 (2002) 1623-1648.

- [11] N.T. Nguyen, T.Q. Bui, C. Zhang, T.T. Truong, Crack growth modeling in elastic solids by the extended meshfree Galerkin radial point interpolation method, *Eng. Anal. Bound. Elem.* 44 (2014) 87-97.
- [12] S. Tanaka, H. Suzuki, S. Sadamoto, M. Imachi, T.Q. Bui, Analysis of cracked shear deformable plates by an effective meshfree plate formulation, *Eng. Fract. Mech.* 144 (2015) 142-157.
- [13] S. Tanaka, H. Suzuki, S. Sadamoto, S. Sannomaru, T. Yu, T.Q. Bui, J-integral evaluation for 2D mixed-mode crack problems employing a meshfree stabilized conforming nodal integration method, *Comput. Mech.* 58 (2016) 185-198.
- [14] S. Tanaka, H. Suzuki, S. Sadamoto, S. Okazawa, T.T. Yu, T.Q. Bui, Accurate evaluation of mixed-mode intensity factors of cracked shear-deformable plates by an enriched meshfree Galerkin formulation, *Arch. Appl. Mech.* 87 (2017) 279-298.
- [15] S. Sadamoto, M. Ozdemir, S. Tanaka, K. Taniguchi, T.T. Yu, T.Q. Bui, An effective meshfree reproducing kernel method for buckling analysis of cylindrical shells with and without cutouts, *Comput. Mech.* 59 (2017) 919-932.
- [16] S. Sadamoto, S. Tanaka, K. Taniguchi, M. Ozdemir, T.Q. Bui, C. Murakami, D. Yanagihara, Buckling analysis of stiffened plate structures by an improved meshfree flat shell formulation, *Thin-Walled Struct.* 117 (2017) 303-313.
- [17] J.S. Chen, C.T. Wu, S. Yoon, Y. You, A stabilized conforming nodal integration for Galerkin meshfree methods, *Int. J. Numer. Methods Eng.* 50 (2001) 435-466.
- [18] J.S. Chen, S. Yoon, C.T. Wu, Non-linear version of stabilized conforming nodal integration for Galerkin mesh-free methods, *Int. J. Numer. Methods Eng.* 53 (2002) 2587-2615.
- [19] M. Hillman, J.S. Chen, An accelerated, convergent, and stable nodal integration in Galerkin meshfree methods for linear and nonlinear mechanics, *Int. J. Numer. Methods Eng.* 107 (2016) 603-630.

- [20] J. Chen, L. Wu, S. Du, A modified J integral for functionally graded materials, *Mech. Res. Commun.* 27 (2000) 301-306.
- [21] M.N. Rao, S. Rahman, Mesh-free analysis of cracks in isotropic functionally graded materials, *Eng. Fract. Mech.* 70 (2003) 1-27.
- [22] J. Sladek, V. Sladek, C. Zhang, An advanced numerical method for computing elastodynamic fracture parameters in functionally graded materials, *Comput. Mater. Sci.* 32 (2005) 532-543.
- [23] S. Shams, B. Soltani, The effects of carbon nanotube waviness and aspect ratio on the buckling behavior of functionally graded nanocomposite plates using a meshfree method, *Polym. Compos.* 38 (2015) E531-E541.
- [24] S. Qin, G. Wei, Z. Liu, G. Su, The elastic dynamics analysis of FGM using a meshless RRPKM, *Eng. Anal. Bound. Elem.* 129 (2021) 125-136.
- [25] T.Q. Bui, N.T. Nguyen, L.V. Lich, M.N. Nguyen, T.T. Truong, Analysis of transient dynamic fracture parameters of cracked functionally graded composites by improved meshfree methods, *Theor. Appl. Fract. Mech.* 96 (2018) 642-657.
- [26] M. Ozdemir, M. Imachi, S. Tanaka, S. Oterkus, E. Oterkus, A comprehensive investigation on macro-micro crack interactions in functionally graded materials using ordinary-state based peridynamics, *Compos. Struct.* 287 (2022) 115299.
- [27] M. Imachi, S. Tanaka, T.Q. Bui, Mixed-mode dynamic stress intensity factors evaluation using ordinary state-based peridynamics, *Theor. Appl. Fract. Mech.* 93 (2018) 97-104.
- [28] M. Imachi, S. Tanaka, T.Q. Bui, S. Oterkus, E. Oterkus, A computational approach based on ordinary state-based peridynamics with new transition bond for dynamic fracture analysis, *Eng. Fract. Mech.* 206 (2019) 359-374.
- [29] M. Imachi, S. Tanaka, M. Ozdemir, T.Q. Bui, S. Oterkus, E. Oterkus, Dynamic crack arrest analysis by ordinary state-based peridynamics, *Int. J. Fract.* 221 (2020) 155-169.

- [30] S.J. Hollister, N. Kikuchi, Homonization theory and digital imaging: A basis for studying the mechanics and design principles of bone tissue, *Biotechnol. Bioeng.* 43 (1994) 586-596.
- [31] K. Koro, K. Abe, Non-orthogonal spline wavelets for boundary element analysis, *Eng. Anal. Bound. Elem.* 25 (2001) 149-164.
- [32] Y.H. Zhou, J. Zhou, A modified wavelet approximation for multi-resolution AWCN in simulating nonlinear vibration of MDOF systems, *Comput. Methods Appl. Mech. Eng.* 197 (2008) 1466-1478.
- [33] Y. Liu, Y. Liu, Z. Cen, Daubechies wavelet meshless method for 2-D elastic problems, *Tsinghua Sci. Technol.* 13 (2008) 605-608.
- [34] D. Wu, K. He, X. Ye, Meshless method based on wavelet function, in: Z. Qian, L. Cao, W. Su, T. Wang, H. Yang (Eds.), *Recent Advances in Computer Science and Information Engineering, Lecture Notes in Electrical Eng.* (2012) 755-760.
- [35] X. Liu, Y. Zhou, X. Wang, J. Wang, A wavelet method for solving a class of nonlinear boundary value problems, *Commun. Nonlinear Sci. Numer. Simul.* 18 (2013) 1939-1948.
- [36] B. Li, X. Chen, Wavelet-based numerical analysis: A review and classification, *Finite Elem. Anal. Des.* 81 (2014) 14-31.
- [37] Y.H. Zhou, Wavelet-Based solutions for linear boundary-value problems, in: *Wavelet Numerical Method and Its Applications in Nonlinear Problems*, *Eng. Appl. Comput. Methods* (2021) 159-179.
- [38] J. Ma, J. Xue, S. Yang, Z. He, A study of the construction and application of a Daubechies wavelet-based beam element, *Finite Elem. Anal. Des.* 39 (2003) 965-975.
- [39] X. Chen, S. Yang, J. Ma, Z. He, The construction of wavelet finite element and its application, *Finite Elem. Anal. Des.* 40 (2004) 541-554.
- [40] A.R. Díaz, A wavelet-Galerkin scheme for analysis of large-scale problems on simple domains, *Int. J. Numer. Methods Eng.* 44 (1999) 1599-1616.

- [41] C.G.A. DeRose Jr, A.R. Díaz, Solving three-dimensional layout optimization problems using fixed scale wavelets, *Comput. Mech.* 25 (2000) 274-285.
- [42] P. Venini, P. Morana, An adaptive wavelet-Galerkin method for an elastic-plastic-damage constitutive model: 1D problem, *Comput. Methods Appl. Mech. Eng.* 190 (2001) 5619-5638.
- [43] G.W. Jang, J.E. Kim, Y.Y. Kim, Multiscale Galerkin method using interpolations wavelets for two-dimensional elliptic problems in general domains, *Int. J. Numer. Methods Eng.* 59 (2004) 225-253.
- [44] S. Tanaka, H. Okada, S. Okazawa, A wavelet Galerkin method employing B-spline bases for solid mechanics problems without the use of fictitious domain, *Comput. Mech.* 50 (2012) 35-48.
- [45] S. Tanaka, H. Okada, S. Okazawa, M. Fujikubo, Fracture mechanics analysis using the wavelet Galerkin method and extended finite element method, *Int. J. Numer. Methods Eng.* 93 (2013) 1082-1108.
- [46] C.K. Chui, J.Z. Wang, A cardinal spline approach to wavelet, *Proc. Am. Math. Soc.* 113 (1991) 785-793.
- [47] T. Belytschko, T. Black, Elastic crack growth in finite elements with minimal remeshing, *Int. J. Numer. Meth. Eng.* 45 (1999) 601-620.
- [48] S. Tanaka, H. Suzuki, S. Ueda, S. Sannomaru, An extended wavelet Galerkin method with a high-order B-spline for 2D crack problems, *Acta Mech.* 226 (2015) 2159-2175.
- [49] S. Tanaka, S. Sannomaru, M. Imachi, S. Hagihara, S. Okazawa, H. Okada, Analysis of dynamic stress concentration problems employing spline-based wavelet Galerkin method, *Eng. Anal. Bound. Elem.* 58 (2015) 129-139.
- [50] H. Wang, S. Tanaka, S. Oterkus, E. Oterkus, Fracture parameter investigations of functionally graded materials by using ordinary state based peridynamics, *Eng. Anal. Bound. Elem.* 139 (2022) 180-191.
- [51] A. Khosravifard, M.R. Hematiyan, A new method for meshless integration in 2D and 3D Galerkin meshfree methods, *Eng. Anal. Bound. Elem.* 34 (2010) 30-40.

- [52] A. Khosravifard, M.R. Hematiyan, L. Marin, Nonlinear transient heat conduction analysis of functionally graded materials in the presence of heat sources using an improved meshless radial point interpolation method, *Appl. Math. Model.* 35 (2011) 4157-4174.
- [53] N.T. Nguyen, T.Q. Bui, M.N. Nguyen, T.T. Truong, Meshfree thermo-mechanical crack growth simulations with new numerical integration scheme, *Eng. Fract. Mech.* 235 (2020) 107121.
- [54] J.R. Rice, A path independent integral and the approximate analysis of strain concentration by notches and cracks, *ASME. J. Appl. Mech.* 35 (1968) 379-386.
- [55] F.Z. Li, C.F. Shih, A. Needleman, A comparison of methods for calculating energy release rates, *Eng. Fract. Mech.* 21 (1985) 405-421.
- [56] I.S. Raju, K.N. Shivakumar, An equivalent domain integral method in the two-dimensional analysis of mixed mode crack problems, *Eng. Fract. Mech.* 37 (1990) 707-725.
- [57] M.L. William, On the stress distribution at the base of a stationary crack, *ASME. J. Appl. Mech.* 24 (1957) 109-114.
- [58] J. Chessa, H. Wang, T. Belytschko, On the construction of blending elements for local partition of unity enriched finite elements, *Int. J. Numer. Methods Eng.* 57 (2003) 1015-1038.
- [59] R. Gracie, H. Wang, T. Belytschko, Blending in the extended finite element method by discontinuous Galerkin and assumed strain methods, *Int. J. Numer. Methods Eng.* 74 (2008) 1645-1669.
- [60] K. Shibamura, T. Utsunomiya, S. Aihara, Correction of incompleteness of XFEM Approximation (2nd report: Application to fracture mechanics), *Trans. of JSCES* (2011) 20110007. (in Japanese)
- [61] <https://www.code-aster.org/spip.php?rubrique2> [accessed 6.9.2022].
- [62] S. Geniaut, P. Massin, N. Moës, Evaluation of stress intensity factors with G-theta method and level sets in *Code_Aster*, 11th International Conference of Fracture, Turin, Italy, 2005.

- [63] H. Wang, S. Tanaka, S. Oterkus, E. Oterkus, Study on two-dimensional mixed-mode fatigue crack growth employing ordinary state-based peridynamics, *Theor. Appl. Fract. Mech.* 124 (2023) 103761.
- [64] P. Underwood, Dynamic relaxation, in: T. Belytschko, T.J.R. Hughes (Eds.), *Computational Methods for Transient Analysis*, North-Holland, Amsterdam (1983) 245-265.
- [65] B. Kilic, E. Madenci, An adaptive dynamic relaxation method for quasi-static simulations using the peridynamic theory, *Theor. Appl. Fract. Mech.* 53 (2010) 194-204.
- [66] H. Ren, X. Zhuang, T. Rabczuk, A new peridynamic formulation with shear deformation for elastic solid, *J. Micromechanics Mol. Phys.* 1 (2016) 1650009.
- [67] E. Madenci, A. Barut, N. Phan, Bond-based peridynamics with stretch and rotation kinematics for opening and shearing modes of fracture, *J. Peridyn. Nonlocal Model.* 3 (2021) 211-254.
- [68] M. Bhandari, K. Purohit, Dynamic fracture analysis of functionally graded material structures - A critical review, *Compos. Part C: Open Access.* 7 (2022) 100227.
- [69] A. Kidane, V.B. Chalivendra, A. Shukla, R. Chona, Mixed-mode dynamic crack propagation in graded materials under thermo-mechanical loading, *Eng. Fract. Mech.* 77 (2010) 2864-2880.
- [70] V. Parameswaran, A. Shukla, Crack-tip stress fields for dynamic fracture in functionally gradient materials, *Mech. Mater.* 31 (1999) 579-596.
- [71] D.D. Nguyen, M.N. Nguyen, N.D. Duc, T.Q. Bui, Modeling the transient dynamic fracture and quasi-static crack growth in cracked functionally graded composites by the extended four-node gradient finite elements, *Compos. Struct.* 284 (2022) 115056.
- [72] A. Candaş, E. Oterkus, C.E. İmrak, Peridynamic simulation of dynamic fracture in functionally graded materials subjected to impact load, *Eng. Comput.* 39 (2023) 253-267.

- [73] Y. Li, T.T. Yu, S. Natarajan, T.Q. Bui, A dynamic description of material brittle failure using a hybrid phase-field model enhanced by adaptive isogeometric analysis, *Eur. J. Mech. Solid.* 97 (2023) 104783.